The Astrophysical Journal, 774:107 (16pp), 2013 September 10 doi:10.1088/0004-637X/774/2/107

DISTANCE AND PROPER MOTION MEASUREMENT OF THE RED SUPERGIANT, PZ CAS, IN VERY LONG BASELINE INTERFEROMETRY H_2O MASER ASTROMETRY

K. Kusuno[1], Y. Asaki[1,2], H. Imai[3], and T. Oyama[4]
[1] Department of Space and Astronautical Science, School of Physical Sciences, The Graduate University for Advanced Studies (SOKENDAI), 3-1-1 Yoshinodai, Chuou-Ku, Sagamihara, Kanagawa 252-5210, Japan; kusuno@vsop.isas.jaxa.jp
[2] Institute of Space and Astronautical Science, 3-1-1 Yoshinodai, Chuou-Ku, Sagamihara, Kanagawa 252-5210, Japan; asaki@vsop.isas.jaxa.jp
[3] Department of Physics and Astronomy, Graduate School of Science and Engineering, Kagoshima University, 1-21-35 Korimoto, Kagoshima 890-0065, Japan; hiroimai@sci.kagoshima-u.ac.jp
[4] Mizusawa VLBI Observatory, National Astronomical Observatory of Japan, 2-21-1 Osawa, Mitaka, Tokyo 181-8588, Japan; t.oyama@nao.ac.jp

Received 2012 November 28; accepted 2013 July 8; published 2013 August 21

ABSTRACT

We present the very long baseline interferometry H_2O maser monitoring observations of the red supergiant, PZ Cas, at 12 epochs from 2006 April to 2008 May. We fitted maser motions to a simple model composed of a common annual parallax and linear motions of the individual masers. The maser motions with the parallax subtracted were well modeled by a combination of a common stellar proper motion and a radial expansion motion of the circumstellar envelope. We obtained an annual parallax of 0.356 ± 0.026 mas and a stellar proper motion of $\mu_\alpha^* \cos\delta = -3.7 \pm 0.2$ and $\mu_\delta^* = -2.0 \pm 0.3$ mas yr^{-1} eastward and northward, respectively. The annual parallax corresponds to a trigonometric parallax of $2.81^{+0.22}_{-0.19}$ kpc. By rescaling the luminosity of PZ Cas in any previous studies using our trigonometric parallax, we estimated the location of PZ Cas on a Hertzsprung–Russell diagram and found that it approaches a theoretically evolutionary track around an initial mass of $\sim 25\ M_\odot$. The sky position and the distance to PZ Cas are consistent with the OB association, Cas OB5, which is located in a molecular gas super shell. The proper motion of PZ Cas is close to that of the OB stars and other red supergiants in Cas OB5 measured by the *Hipparcos* satellite. We derived the peculiar motion of PZ Cas of $U_s = 22.8 \pm 1.5$, $V_s = 7.1 \pm 4.4$, and $W_s = -5.7 \pm 4.4$ km s^{-1}. This peculiar motion has rather a large U_s component, unlike those of near high-mass star-forming regions with negatively large V_s motions. The uniform proper motions of the Cas OB5 member stars suggest random motions of giant molecular clouds moving into local potential minima in a time-dependent spiral arm, rather than a velocity field caused by the spiral arm density wave.

Key words: Galaxy: structure – masers – supergiants

Online-only material: color figures

1. INTRODUCTION

Recent very long baseline interferometry (VLBI) astrometry can determine distances to Galactic objects on the kiloparsec scale. One of these objects is a red supergiant (RSG) harboring a thick circumstellar envelope. Since those sources radiate water masers in the radio frequency (RF), we can measure trigonometric parallaxes by referring distant extragalactic radio sources using a phase-referencing technique (e.g., Hachisuka et al. 2006). If we can measure the trigonometric parallax distance of such a star, this enables us to evaluate the absolute magnitude. Since the location of an RSG in an evolutionary track of a Hertzsprung–Russell (H-R) diagram is not mainly dependent on an effective temperature, we can make a constraint on the initial mass from the absolute magnitude (Choi et al. 2008). In addition, because RSGs are sometimes seen in large OB associations in the Milky Way, they can become distance indicators for such OB associations. Determining trigonometric rather than photometric distances to OB associations is important for the verification of the calibration method of the distance ladder.

Information about trigonometric parallaxes and proper motions, together with radial velocities, also enables us to investigate the three-dimensional (3D) motions of the stars in the Milky Way. Because proper motions of the water masers around RSGs can be well fitted to a simple expanding flow even with some inhomogeneity in it, which is different from the case of star-forming regions, the proper motion of a mass center of an RSG can be rather easily estimated from the phase-referencing VLBI. Asaki et al. (2010) obtained the 3D motion of an RSG, S Per, and found it to have a relatively large deviation (15 km s^{-1}) from the motion expected from a flat Galactic rotation curve. Considering the age of S Per is a few tens of million years, it is difficult to have a large peculiar motion that old stars often have. However, it is quite important to know whether or not RSGs' motions are aligned with their accompanying OB associations for further discussions about Milky Way dynamics. Asaki et al. (2010) pointed out that since S Per is involved in the Per OB1 association, such a large peculiar motion of an OB association member star may be related to a dynamics and mechanism of the spiral arm formation of the Milky Way (Baba et al. 2009).

Here we report on results of phase-referencing VLBI monitoring observations of the H_2O masers associated with another RSG, PZ Cas, conducted over two years with the VLBI Exploration of Radio Astrometry (VERA) of the National Astronomical Observatory of Japan (NAOJ). These observations are described in Section 2. Data reduction including astrometric analyses is presented in Section 3. Astrometric results of PZ Cas are presented in Section 4. We discuss the results in Section 5. For Sections 2–4, we adopt a solar motion of 20 km s^{-1} (Kerr & Lynden-Bell 1986) relative to the local standard of rest (LSR) to the direction of $(\alpha_{1900}, \delta_{1900}) = (18^{\rm h}, 30^\circ)$. Hereafter this solar motion is referred to as the standard solar motion. With the standard solar motion, the systemic velocity of PZ Cas is -36.16 km s^{-1}, calculated from the heliocentric

Table 1
Observing Epochs of PZ Cas Astrometric Monitoring Observations

Epoch	Date	Time Range (UTC)
A	2006 Apr 20	19:41–05:20
B	2006 Jul 14	14:21–23:10
C	2006 Aug 13	12:21–21:35
D	2006 Oct 19	08:01–17:20
E	2006 Dec 13	04:21–13:40
F	2007 Mar 22	00:21–08:17
G[a]	2007 May 2	18:51–04:40
H[b]	2007 Jul 25	13:20–23:04
I[c]	2007 Sep 19	10:20–20:10
J	2007 Nov 7	07:20–17:10
K	2007 Dec 22	04:25–14:15
L	2008 May 12	19:00–04:50

Notes.
[a] Signal-to-noise ratio for all the baselines was unexpectedly low.
[b] T_{sys} data of ISHIGAKI was used in place of OGASA20.
[c] IRIKI did not attend the observation.

Table 2
Frequency Allocation for PZ Cas and J2339+6010 at Epoch F

Beam	A	B
Source	PZ Cas	J2339+6010
Base band number	1	14
Frequency range (GHz)	22.234–22.242	22.106–22.122
		22.122–22.138
		22.138–22.154
		22.154–22.170
		22.170–22.186
		22.186–22.202
		22.202–22.218
		22.234–22.250
		22.250–22.266
		22.266–22.282
		22.282–22.298
		22.298–22.314
		22.314–22.330
		22.330–22.346
Frequency spacing	15.625 kHz[a] (512 channels)	250.0 kHz (64 channels)

Note. [a] The velocity spacing of the A beam for the H_2O masers is $0.2107\,\mathrm{km\,s^{-1}}$.

radial velocity of $-45.68 \pm 0.68\,\mathrm{km\,s^{-1}}$ (Famaey et al. 2005). On the other hand, we discuss the observational results on the basis of the solar motion reported by Schönrich et al. (2010) in Section 5.3. For the proper motion, we adopt the heliocentric coordinates.

2. OBSERVATIONS

VLBI phase-referencing observations of PZ Cas at 22.2 GHz have been conducted at 12 epochs over two years with four VERA antennas at Mizusawa, Iriki, Ogasawara, and Ishigakijima (coded as MIZNAO20, IRIKI, OGASA20, and ISHIGAKI, respectively). The observing epochs are listed in Table 1.

The VERA antennas have a dual beam receiving system each to observe a closely located pair of sources simultaneously (Honma et al. 2003). In our monitoring program, one beam (beam A) observed PZ Cas and another (beam B) observed a closely located continuum source, J233921.1+601011 (hereafter abbreviated to J2339+6010), which was one of the VERA 22 GHz calibrator survey sources (Petrov et al. 2007) 1°.7 away and used as a position reference. The observation duration was 8–10 hr. Each observation was divided into several sessions for the simultaneous tracking of PZ Cas and J2339+6010, each separated by short-term sessions of bright calibrators (3C 454.3 and J230043.0+165514) for 15 minutes in order to check the observing systems. We prepared one baseband channel (BBC) with a bandwidth of 16 MHz for PZ Cas and fourteen BBCs with a total bandwidth of 224 MHz for J2339+6010 in left-hand circular polarization. VLBI cross-correlation was carried out with the Mitaka FX correlator at NAOJ, Mitaka, Japan, to produce VLBI fringe data with 512 spectral channels for PZ Cas for the central 8 MHz bandwidth, corresponding to a velocity spacing of $0.2107\,\mathrm{km\,s^{-1}}$ for the H_2O $J_{K_-K_+} = 6_{16}$–5_{23} maser line. A typical frequency allocation after the cross-correlation is listed in Table 2.

3. DATA REDUCTION

To describe the phase referencing and imaging analysis process, we often refer to the results of a specific epoch observation (epoch F on 2007 March 22) because we started the data analysis with this epoch data. We analyzed the VLBI data using the standard NRAO data reduction software, Astronomical Image Processing Software (AIPS), version 31DEC10.

3.1. Initial Calibrations

Initial calibration tasks were common for both the sources. First, the amplitude calibration was carried out by using the system noise temperatures (T_{sys}) and gain calibration data. The measurements of T_{sys} often have abrupt time variations, as shown in Figure 1, especially when rain falls happened during the observation. We consider such rapid and abrupt time variations to be caused by the absorption effect of water puddles on the top of the VERA antenna feedome. We carried out a polynomial fitting of the raw T_{sys} data after removing such abrupt changes. At epoch H, since T_{sys} was not recorded for either beams A or B of the ISHIGAKI station. Instead, T_{sys} of OGASA20 was used for ISHIGAKI, because the atmospheric environment (temperature and moisture) is similar. Note that minor amplitude calibration errors at this stage can be approximately corrected in the later self-calibration. The system noise temperatures for beams A and B were basically approximated to be identical, so the time variation of the system noise temperature must be mainly attributed to the common atmosphere.

In the next step, the two-bit sampling bias in the analog-to-digital (A/D) conversion in VLBI signal processing was corrected. Earth-orientation-parameter (EOP) errors, ionospheric dispersive delays, and tropospheric delays were calibrated by applying precise delay tracking data calculated with an updated VLBI correlator model supplied by the NAOJ VLBI correlation center. The instrumental path differences between the two beams were corrected using the post-processing calibration data supplied by the correlation center (Honma et al. 2008). The phase-tracking centers for PZ Cas and J2339+6010 of the updated correlator model were set to the positions given in Table 3 for all the observing epochs.

3.2. Phase Referencing and Imaging

After the initial calibration, an image of the reference source, J2339+6010, was synthesized using the standard VLBI imaging method with the fringe fitting and self-calibration. We carried

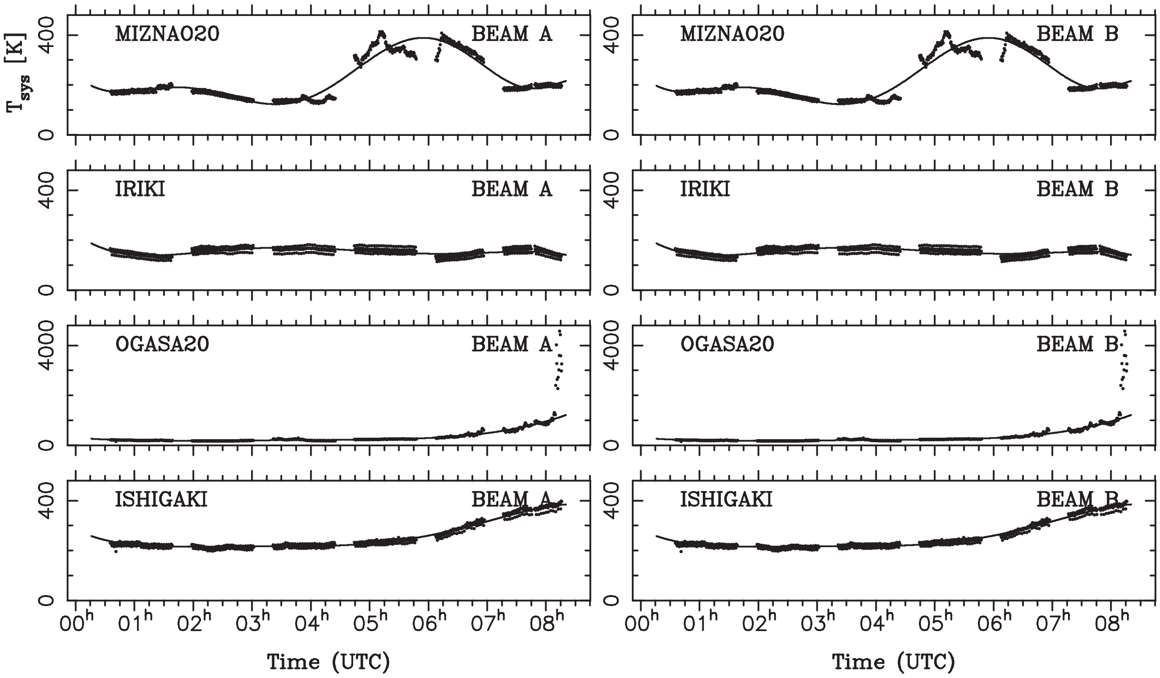

Figure 1. System noise temperature at epoch F. The abscissa is time in UTC and the ordinate is the system noise temperature in kelvin. The dotted points are measurements and the solid lines are the polynomial fitting curves after removing the abrupt changes. The left and right panels show beams A and B, respectively. From the top to bottom plots: MIZNAO20, IRIKI, OGASA20, and ISHIGAKI stations.

Table 3
Phase Tracking Center Positions of the Observed Sources

	Right Ascension (J2000)	Declination (J2000)
PZ Cas	$23^{\rm h}44^{\rm m}03^{\rm s}.281900$	$+61^\circ47'22''.182000$
J2339+6010	$23^{\rm h}39^{\rm m}21^{\rm s}.125210$	$+60^\circ10'11''.849000$

out the above process twice to make the image of J2339+6010: the first process started with a single point source model and the second with the reference source image that had been made in the previous process. After imaging, the phase-referencing calibration solutions were directly calculated from the reference source fringe data: the calibrating phase, $\Phi_{\rm cal}(t)$, at time t was obtained from the following calculation with a vector average of all the spectral channels in all the BBCs:

$$\exp[i\Phi_{\rm cal}(t)] = \sum_{n=1}^{N}\sum_{m=1}^{M}\exp\big\{i\big[\Phi^{\rm r}_{\rm raw}(n,m,t) + 2\pi\big[\nu^{\rm r}_n + (m-1)\Delta\nu - \nu^{\rm t}_0\big]\Delta\tau^{\rm r}_{\rm g}(t) - \Phi^{\rm r}_{\rm v}(U(t),V(t))\big]\big\},$$

where $\Phi^{\rm r}_{\rm raw}$ is the raw data fringe phase of the reference source and $\Phi^{\rm r}_{\rm v}(U(t),V(t))$ is the visibility phase calculated from the CLEAN components of the reference source image for a baseline with $U(t)$ and $V(t)$. $N = 14$ is the BBC number, $M = 64$ is the spectral channel number in the single BBC, $\nu^{\rm t}_0$ is the RF frequency of the strongest H_2O maser emissions in beam A, $\nu^{\rm r}_n$ is the RF frequency at the lower band edge of the nth BBC for the reference source as listed in Table 2, $\Delta\nu = 250$ kHz is the frequency spacing in the single BBC for the reference source, m is the integer number indicating the order of the frequency channel in the single BBC, and $\Delta\tau^{\rm r}_{\rm g}(t)$ is the third-order polynomial fitting result of the temporal variation of the group delay obtained from the preceded fringe fitting for the reference source. We refer to the phase calibration solutions obtained with this method as direct phase-transfer (DPT) solutions. The DPT solutions were then smoothed by making a running mean with an averaging time of 16 s in order to reduce the thermal noise. The smoothed DPT solutions, as well as the one obtained with an ordinary AIPS phase-referencing analysis (AIPS CL table), are shown in Figure 2. Those two results are basically consistent with each other. Note that even when solutions could not be obtained with the fringe fitting or the following AIPS self-calibration because the signal-to-noise ratios (S/N) was below a cutoff value, the DPT solutions were created from the raw fringe data, as shown for the OGASA20 station in Figure 2. The final astrometric result with the smoothed DPT solutions is consistent with the AIPS CL table at epoch F.

Amplitude gain adjustment was performed using a third-order polynomial fitting for the amplitude self-calibration solutions for J2339+6010. Since S/N of J2339+6010 was unexpectedly low at epoch G, we could not obtain good solutions for J2339+6010 in the fringe fitting. We therefore obtained the group delay solutions from 3C 454.3 and set the amplitude gain to the unity for all the observing time. The DPT solutions were created from the J2339+6010 fringe data together with the group delay solutions determined with 3C 454.3. At epoch I, since IRIKI did not attend the observation, we used the remaining three stations in the data reduction.

The Doppler shift in PZ Cas spectra due to Earth's rotation and revolution was corrected after the phase referencing. The observed frequencies of the maser lines were converted to radial velocities with respect to the traditional LSR using the rest frequency of 22.235080 GHz for the H_2O 6_{16}–5_{23} transition. Since the cross power spectra within the received frequency region showed a good flatness both in the phase and the amplitude, the receiver complex gain characteristics were not calibrated in this analysis. We inspected the cross power spectra for all the baselines in order to select a velocity channel of

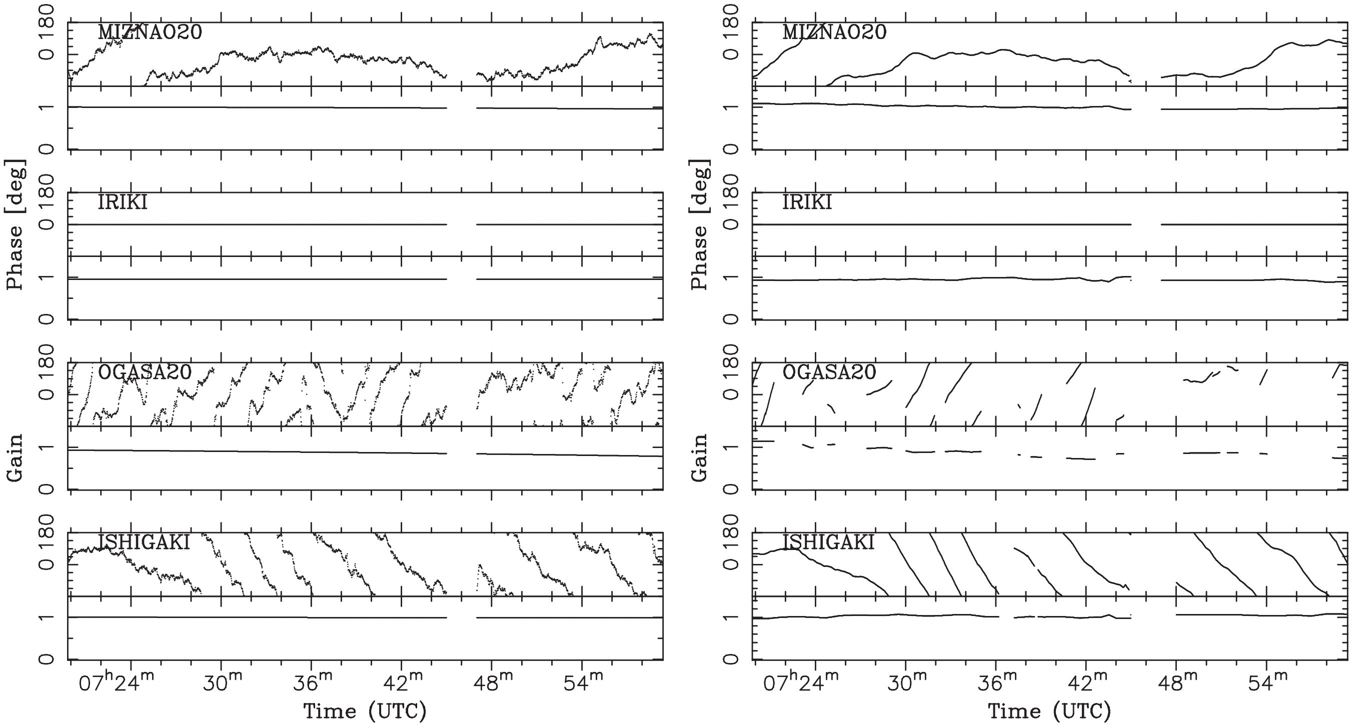

Figure 2. Complex gain calibration solutions obtained from J2339+6010 at epoch F for the phase referencing. IRIKI is the reference antenna. Each antenna has two plots: the abscissa is time in UTC, and the ordinate is the phase calibration data in degree and the amplitude gain for the upper and lower plots, respectively. The left and right plots show the direct phase-transfer (DPT) solutions introduced in Section 3.2 and those obtained in an AIPS phase-referencing analysis (AIPS CL table), respectively. For making the AIPS CL table, the solution intervals were set to 2, 2, and 10 minutes for the fringe fitting, phase-only self-calibration, and amplitude-and-phase self-calibration, respectively. From the top to bottom plots: MIZNAO20, IRIKI, OGASA20, and ISHIGAKI.

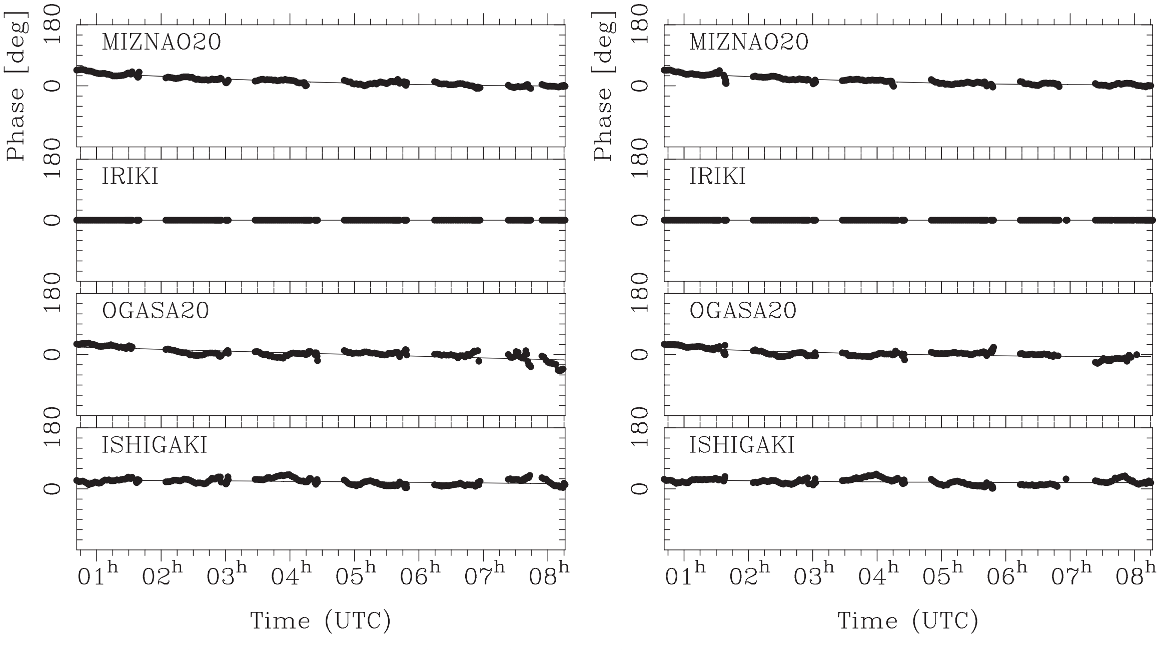

Figure 3. Phase solutions using the fringe fitting with a solution interval of 20 minutes for the PZ Cas's brightest velocity channel ($V_{\rm LSR} = -42.0\,{\rm km\,s^{-1}}$) at epoch F. The abscissa is the time in UTC, and the ordinate is the phase in degree. IRIKI is the reference antenna. The dotted points are the fringe-fitting solutions, and the solid lines represent fitting results with a third-order polynomial for each station. The left and right plots show the fringe-fitting results after the phase referencing with the direct phase-transfer calibration and the AIPS CL table, respectively. From the top to bottom plots: MIZNAO20, IRIKI, OGASA20, and ISHIGAKI.

the maser emission which would be unresolved and not have rapid amplitude variation. At this step, fast phase changes with a typical timescale of a few minutes to a few tens of minutes can be removed by the phase referencing, but slow time variations including a bias component as shown in Figure 3 cannot. The maser image was distorted because of the residual time variations of the fringe phase on a timescale of several hours, which might be caused by uncertainties in the updated VLBI correlator model. We conducted the fringe fitting for the selected velocity channel with a solution interval of 20 minutes. We fitted the solutions to a third-order polynomial, as shown in Figure 3, and removed it from both of the fringe phases of

PZ Cas and J2339+6010. This procedure removes the residual fringe phase error from the PZ Cas data while it is transferred to the J2339+6010 data. As a result, this leads to an improvement of the PZ Cas image quality, but it also creates a distortion of the J2339+6010 image. This distortion of the reference source causes an astrometric error in the relative position between the sources, as later discussed in Section 3.3.

Figure 3 also shows the fringe phase residuals obtained with the AIPS CL table. Although the fringe-fitting results with the AIPS CL table can be almost identifiable to those with the DPT solutions, it is later noted that the image peak flux density at $V_{\rm LSR} = -42.0\,{\rm km\,s^{-1}}$ with the DPT solutions is 2% lower than that with the AIPS CL table at epoch F. In addition, the image rms noise resulting from the DPT solutions is 5% higher than that resulting from the AIPS CL table. We can also see that the residual phases resulting from the DPT solutions in the fifth and sixth observing sessions in Figure 3 have a larger deviation than those resulting from the AIPS CL table. Although the number of the calibrated visibilities after applying the DPT solutions was larger than that with the AIPS CL table, especially in the last two sessions, the visibilities with lower S/N might degrade the final image quality. We have to admit that the AIPS CL table may lead to a slightly higher quality in the image synthesis because the fringe fitting and self-calibration take off visibility with low S/N. The problem is that there were some observations whose data showed unexpectedly low S/N for certain baselines. For such cases, it was hard to create the AIPS CL table with the fringe fitting and self-calibration. For the following three reasons, we used the DPT solutions instead of the AIPS CL table for all the observing epochs: (1) the DPT is useful even when the fringe fitting fails because of the low S/N, (2) the final astrometric results between the two methods have little difference, and (3) it is preferable to use a unified analysis scheme for obtaining scientific results from a data set with the same (U, V) distribution.

The DPT solutions and the long-term phase calibration data were applied to the remaining frequency channels to make image cubes for the LSR velocity range of -23.0 to $-60.8\,{\rm km\,s^{-1}}$ with a step of $0.2107\,{\rm km\,s^{-1}}$. Image synthesis with 60 μas pixel for a region of 4096 × 4096 pixels, roughly a 246 × 246 square milliarcsecond (mas) region, was made by using IMAGR. To initially pick up maser emissions in the maps, we used the AIPS two-dimensional (2D) Gaussian component survey task, SAD, in each velocity channel map in order to survey emissions. We visually inspected the surveyed Gaussian components one by one. We stored the image pixels that were larger than a 5σ noise level for a visually confirmed maser emission. Hereafter we define a maser "spot" as an emission in a single velocity channel, and a maser "feature" as a group of spots observed in at least two consecutive velocity channels at a coincident or very closely located positions.

3.3. Accuracy of the Relative Position of PZ Cas

In the phase-referencing astrometric analysis, positions of the PZ Cas maser spots were obtained with respect to that of the J2339+6010 image. The positional error includes the effect of a peak position shift due to uncertainties in the VLBI correlator model (atmospheric excess path lengths [EPLs], antenna positions, EOP, and so on) for the sources. Hereafter we refer to the relative position error of a pair of point sources using the phase referencing due to uncertainties in a VLBI correlator model as an astrometric error.

We conducted Monte Carlo simulations of phase-referencing observations for the pair of PZ Cas and J2339+6010 to estimate the astrometric error. For generating simulated phase-referencing fringes, we used an improved version of a VLBI observation simulator, ARIS (Astronomical Radio Interferometer Simulator; Asaki et al. 2007), with new functions simulating station clocks (Rioja et al. 2012) and amplitude calibration errors. In the simulations, we assumed flux densities of PZ Cas and J2339+6010 of equivalently 10 Jy and 0.2 Jy for 15.6 kHz and 224 MHz bandwidths, respectively, which were determined from our observations. The sources were assumed to be point sources. The observation schedule and observing system settings in the simulations, such as the recording bandwidth and A/D quantization level, were adopted from the actual VERA observations. A tropospheric zenith EPL error of 2 cm and other parameters were set as suggested for VERA observations (Honma et al. 2010). For simplification of the simulations, reference source position errors were not considered. The simulation results from 200 trials are shown in Figure 4. They show that the 1σ errors in the relative position are 72 and 33 μas in right ascension and declination, respectively. We used these standard deviations as the astrometric error in the following analysis.

At epoch I, the IRIKI station geographically located at the center of the VERA could not attend the observation, so the astrometric accuracy may become worse with the remaining three stations. We conducted another simulation series for the three-station case, and the resultant astrometric accuracy is 101 and 39 μas for right ascension and declination, respectively. We therefore used this astrometric accuracy at epoch I in the following analysis.

4. RESULTS

Maser features of PZ Cas are spatially distributed over a region of 200 × 200 square mas. We identified 52 maser spots that are assembled into 16 maser features. Those maser features were arranged in 11 maser groups, which are labeled *a* to *k*, as shown in Figure 5. Groups *a* to *e*, and *g*, *h*, and *i* have a radial velocity range between -51.9 and $-40.5\,{\rm km\,s^{-1}}$. Groups *f*, *j*, and *k*, which have been detected at one epoch, have a radial velocity of -52.3, -39.3, and $-37.6\,{\rm km\,s^{-1}}$, respectively. The radial velocities of the identified maser spots are close to the stellar systemic velocity ($V_{\rm LSR} = -36.16 \pm 0.68\,{\rm km\,s^{-1}}$). Groups *a* and *b* located to the north and southeast of the spatial distribution, respectively, are bright and have complicated structures, while the other groups (*c* to *k*) have a rather simple structure. For the following annual parallax analysis, we selected 16 maser spots among 52 using the following two criteria. (1) Maser spots were detected with the image S/N greater than or equal to 7. (2) The maser spot was detected at eight epochs or more. All the selected maser spots belong to either group *a* or *b* by chance.

4.1. Annual Parallax

In the first step of the annual parallax analysis, we performed a Levenberg–Marquardt least-squares model fitting of the maser motions in the same way as that described by Asaki et al. (2010) using the peak positions of the selected maser spots. We adopted the astrometric error as mentioned in Section 3.3 and a tentative value of a morphology uncertainty (a positional uncertainty due to maser morphology variation) of 50μas in the fitting, equivalent to 0.1 AU by assuming the distance of 2 kpc to the source. Figures 6 and 7 show the images and

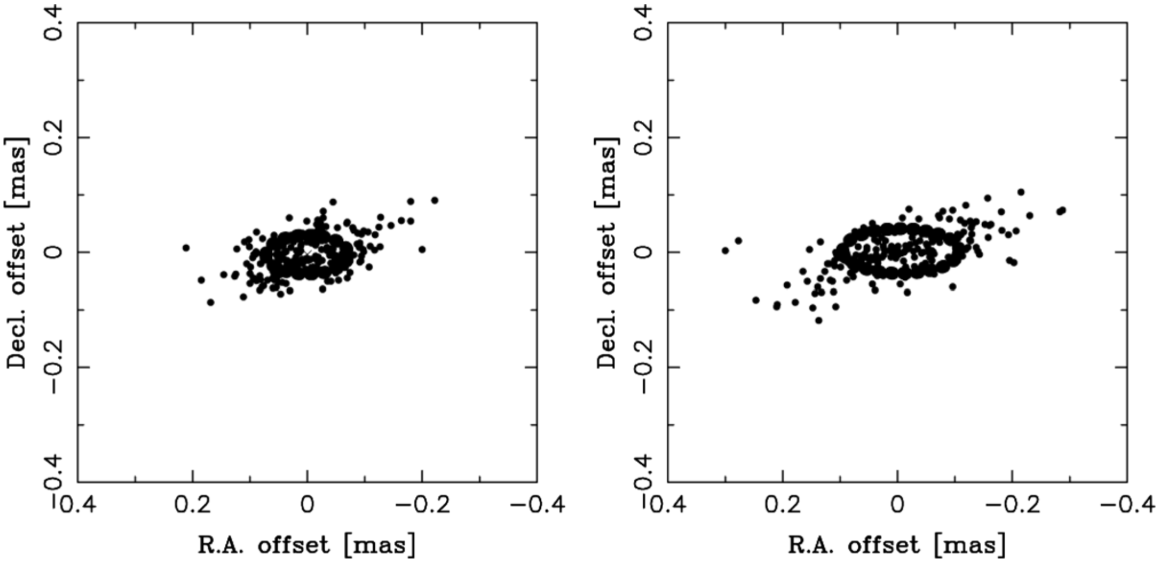

Figure 4. Astrometric observation simulation results for the pair of PZ Cas and J2339+6010. The dots represent PZ Cas's image peak positions relative to J2339+6010 at 22 GHz with the VERA for 200 trials. The ellipses represent 1σ for the distributions. Left: the VERA full array case. Right: the VERA three-station case (MIZNAO20, OGASA20, and ISHIGAKI).

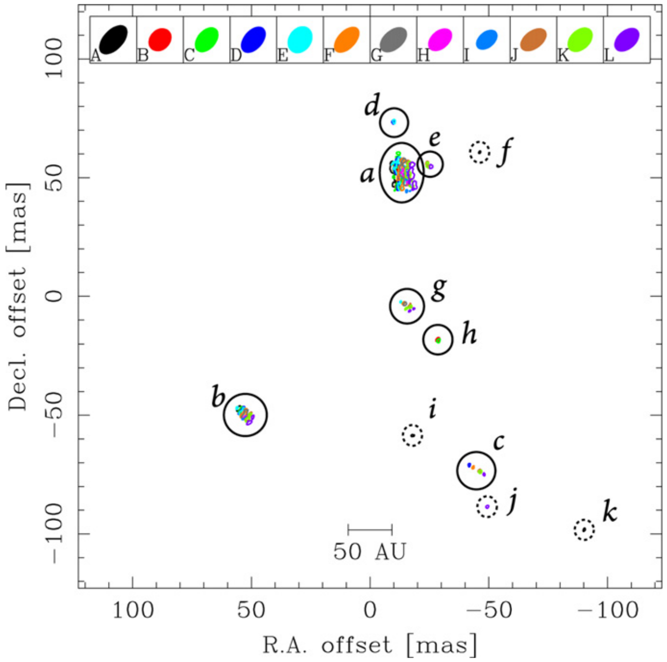

Figure 5. Spatial distribution of the PZ Cas H_2O masers in the 12 epochs. The outlines of maser features represent a 5σ noise-level contour (418, 722, 661, 367, 467, 344, 309, 658, 686, 440, 313, and 285 mJy at epochs A, B, C, D, E, F, G, H, I, J, K, and L, respectively). The synthesized beams are shown in the upper 1×1 square mas boxes. Maser features surrounded with circles represent maser groups. Groups *f*, *i*, *j*, and *k* are features detected at a single epoch. Group *a* is composed of four features. Groups *b* and *g* are composed of two features. The map origin is the phase-tracking center.

the fitting results of all the selected maser spots. The stellar annual parallax, π^*, was determined by the combined fitting with the Levenberg–Marquardt least-squares analysis for all the selected spots. The obtained stellar annual parallax was 0.380 ± 0.011 mas at this stage.

If we carefully look at Figure 7, the maser spots do not seem to be properly identified with the image peak positions because multiple maser spots are spatially blended. This is caused when the multiple maser spots, whose size is typically 1 AU (Reid & Moran 1981), are closely located comparing with the synthesized beam size of ∼1 mas in this case, equivalent to 2.6 AU at the distance of PZ Cas. To identify an individual maser spot properly, especially for blended structures, we performed AIPS JMFIT for the 2D multiple Gaussian component fitting of the emissions. Here we refer to a maser spot that can be identified with the image peak position as an isolated maser spot, and to a maser spot that cannot be identified with a single peak position because of the insufficient spatial resolution as a blended component. If we can identify 2D Gaussian components using JMFIT, instead of SAD that automatically searches multiple spots, in the brightness distribution, we refer to such spots as identified spots. Figure 8 provides an example of the annual parallax least-squares fitting for a maser spot using either the image peak position or the 2D Gaussian peak. Table 4 lists our combined fitting results using the image peak only for the isolated spots, only for the blended components, and for all those involved in the two groups. We also tried to make another combined fitting using the Gaussian peak only for the isolated spots, only for the blended but identified spots with JMFIT, and all of them, as listed in the bottom row in Table 4. The combined fitting results for the isolated spots show little difference between the cases of image peak and Gaussian peak. However, the fitting result for the blended spots with JMFIT peak positions is definitely changed from that with the image peak for the blended components and becomes closer to that obtained with the isolated spots. If a maser spot is recognized as an isolated spot, in other words, if a maser cloud is spatially resolved into multiple spots in the image, the image peak position can be treated as the maser position. Because this cannot be the case for the maser spots of PZ Cas, we adopted the Gaussian peak positions in our least-squares model fitting. The model fitting results obtained from the individual spots are listed in Table 5. From the combined fitting analysis by using all the selected maser spots, we obtained the stellar annual parallax of 0.356 ± 0.011 mas with assumptions of the above astrometric error and morphology uncertainty at this stage.

Although H_2O maser features around RSGs are good tracers for astrometry (Richards et al. 2012), the morphology of

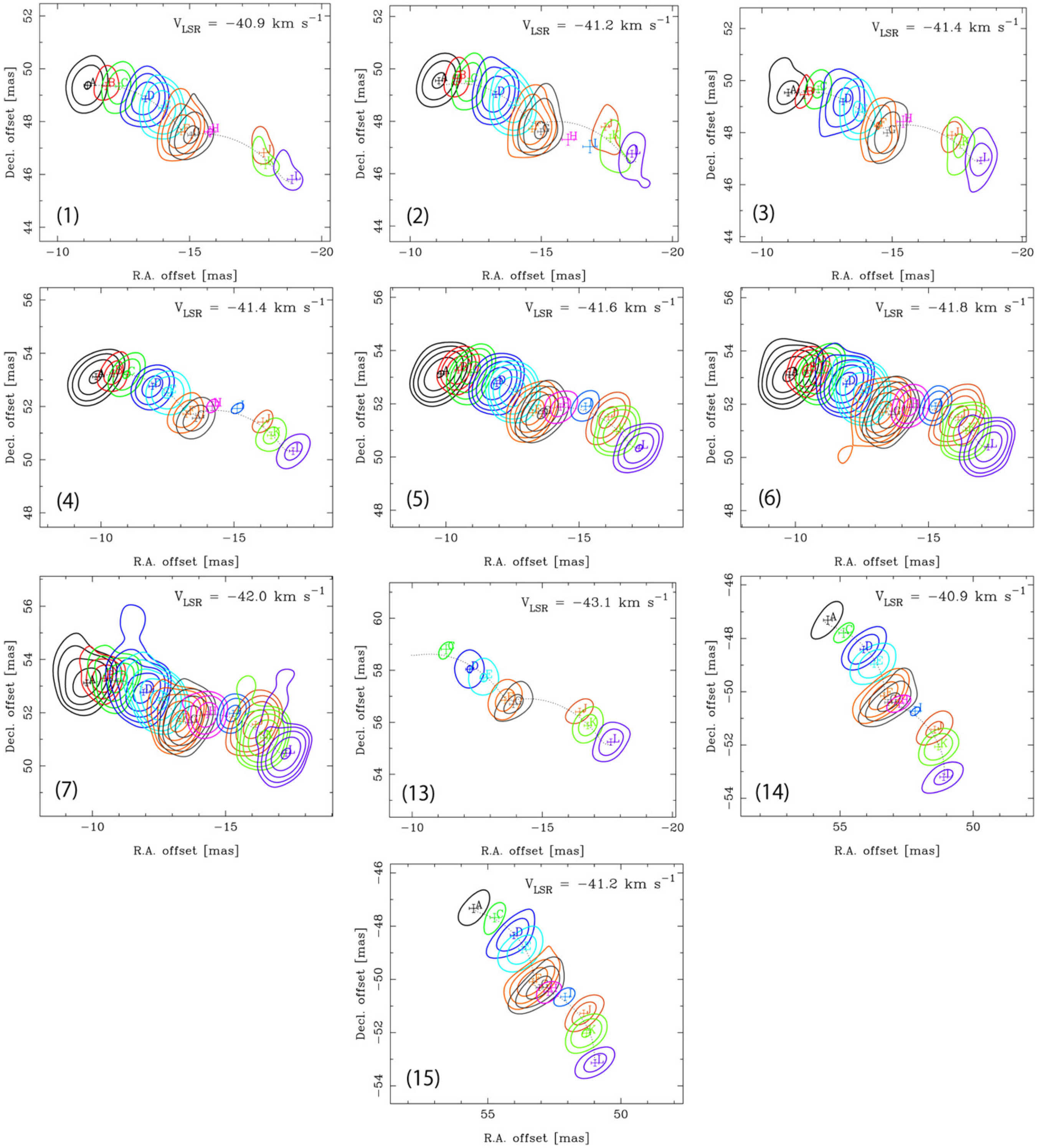

Figure 6. Spatial motions of 10 isolated maser spots. The color represents an observation epoch as shown in Figure 5. The dotted lines represent the best-fit annual parallax and proper motion. The outermost contours show a 5σ noise level increased by a factor of 2. The number at the bottom left corner in each of the panels is the maser spot ID as listed in Table 5. Positional errors are displayed at the image peak positions. The dashed lines represent the least-squares fitting results of the spatial motion of an annual parallax and a linear motion for the maser peak positions.

(A color version of this figure is available in the online journal.)

Table 4
Annual Parallax Results (mas) of PZ Cas

Spot Identification Method	Blended Component	Isolated Component	All
Image peak	0.402 ± 0.021	0.371 ± 0.013	0.380 ± 0.011
2D Gaussian peak	0.352 ± 0.017	0.358 ± 0.013	0.356 ± 0.011

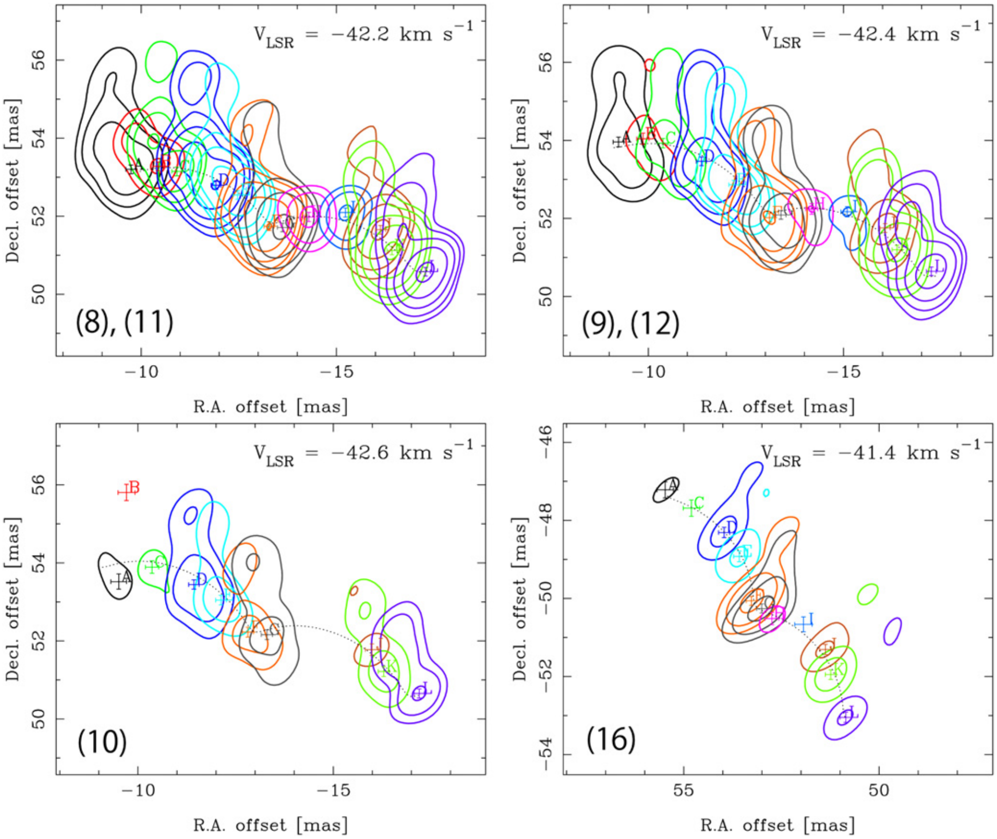

Figure 7. Same as Figure 6, but for the maser spots identified as the blended component. The maser components in the upper two panels have two maser spots while those in the lower panels have a single spot.

(A color version of this figure is available in the online journal.)

Table 5
Proper Motions, Initial Positions, and Parallaxes of the PZ Cas H_2O Maser Spots

Spot ID (Group ID)	$\Delta\alpha_A$ (mas)	$\Delta\delta_A$ (mas)	V_{LSR} (km s^{-1})	π (mas)	$\mu_\alpha \cos\delta$ (mas yr^{-1})	μ_δ (mas yr^{-1})
1(*a*)	−4.24 ± 0.07	52.24 ± 0.03	−40.9	0.324 ± 0.042	−3.79 ± 0.06	−1.66 ± 0.03
2(*a*)	−4.20 ± 0.07	52.40 ± 0.04	−41.2	0.379 ± 0.044	−3.70 ± 0.06	−1.46 ± 0.03
3(*a*)	−4.07 ± 0.07	52.70 ± 0.04	−41.4	0.340 ± 0.044	−3.72 ± 0.06	−1.30 ± 0.03
4(*a*)	−2.77 ± 0.07	56.32 ± 0.04	−41.4	0.380 ± 0.039	−3.67 ± 0.06	−1.34 ± 0.03
5(*a*)	−2.83 ± 0.07	56.29 ± 0.03	−41.6	0.357 ± 0.039	−3.72 ± 0.06	−1.33 ± 0.03
6(*a*)	−2.82 ± 0.07	56.28 ± 0.03	−41.8	0.363 ± 0.038	−3.73 ± 0.06	−1.30 ± 0.03
7(*a*)	−2.83 ± 0.07	56.32 ± 0.03	−42.0	0.357 ± 0.038	−3.76 ± 0.06	−1.30 ± 0.03
8(*a*)	−2.90 ± 0.07	56.32 ± 0.03	−42.2	0.355 ± 0.039	−3.74 ± 0.06	−1.25 ± 0.03
9(*a*)	−2.62 ± 0.07	56.62 ± 0.03	−42.4	0.302 ± 0.039	−3.78 ± 0.06	−1.28 ± 0.03
10(*a*)	−2.49 ± 0.07	56.70 ± 0.04	−42.6	0.355 ± 0.046	−3.95 ± 0.06	−1.53 ± 0.03
11(*a*)	−2.39 ± 0.08	58.82 ± 0.05	−42.2	0.436 ± 0.045	−3.74 ± 0.06	−1.81 ± 0.03
12(*a*)	−2.27 ± 0.07	58.65 ± 0.04	−42.4	0.349 ± 0.043	−3.69 ± 0.06	−1.82 ± 0.03
13(*a*)	−3.14 ± 0.07	61.47 ± 0.04	−43.1	0.357 ± 0.051	−3.81 ± 0.08	−1.62 ± 0.03
14(*b*)	63.82 ± 0.07	−45.57 ± 0.03	−40.9	0.367 ± 0.044	−2.28 ± 0.07	−2.86 ± 0.03
15(*b*)	63.75 ± 0.07	−45.49 ± 0.03	−41.2	0.349 ± 0.041	−2.30 ± 0.07	−2.85 ± 0.03
16(*b*)	63.70 ± 0.07	−45.46 ± 0.04	−41.4	0.335 ± 0.044	−2.32 ± 0.07	−2.84 ± 0.03

the maser spots observed with the high-resolution VLBI is no longer negligible for the precise maser astrometry. These monitoring observations of PZ Cas have been conducted so often for two years that we can investigate the contribution of the morphology uncertainty to the maser astrometry. Figure 9 shows the position residuals of the 16 selected maser spots after removing the stellar annual parallax of 0.356 mas, proper motion, and initial position estimated for each of the spots. The standard deviation of the residuals is 93 and 110 μas for right ascension and declination, respectively. Assuming that those errors have the statistical characteristics of a Gaussian distribution, the morphology uncertainty is $59(=\sqrt{93^2–72^2})$ and $105(=\sqrt{110^2–33^2})$ μas for right ascension and declination, respectively, where 72 and 33 μas are the astrometric errors discussed in Section 3.3. It is unlikely that the morphology uncertainty has different values between right ascension and declination, so we adopted

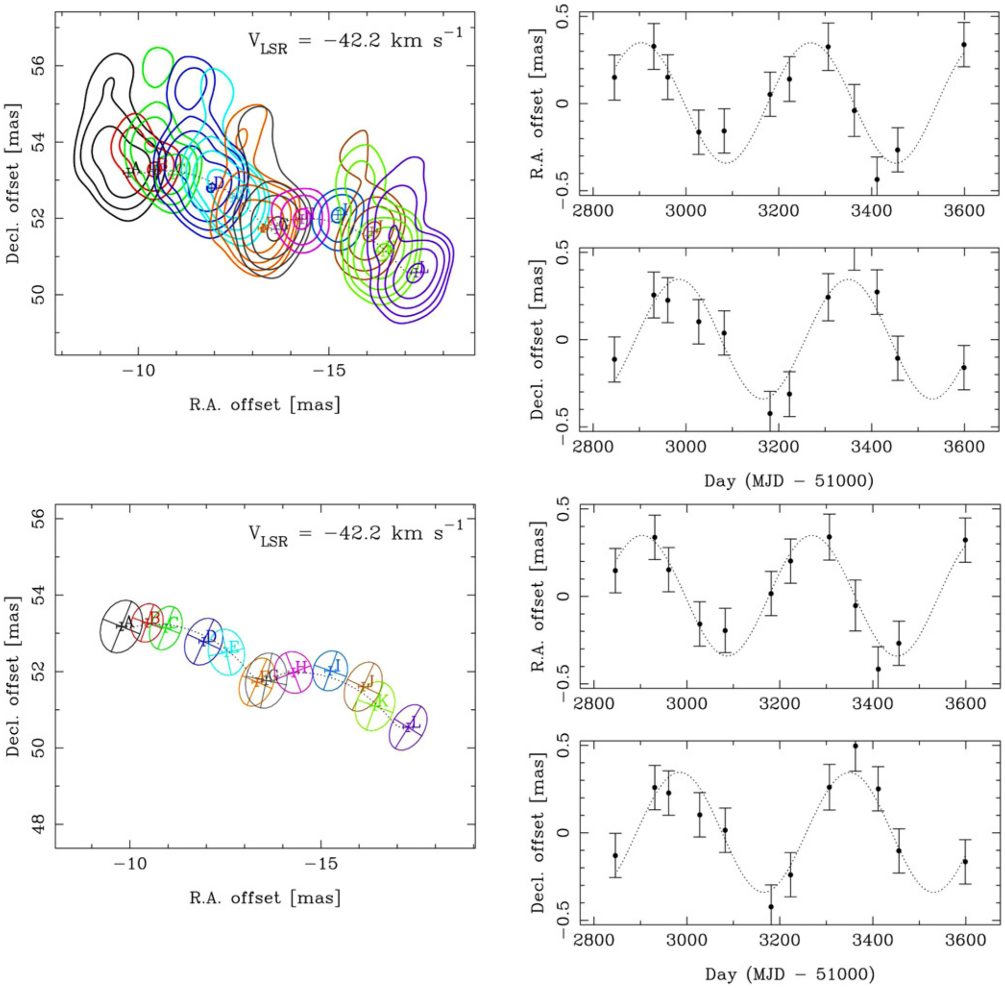

Figure 8. Least-squares fitting results of the motions of the maser spot with the LSR velocity of $-42.2\,\mathrm{km\,s^{-1}}$. Top three panels: least-squares fitting using the image peak positions. Bottom three panels: least-squares fitting using the two-dimensional Gaussian peak positions. The left panels show the maser positions after removing the initial position and the proper motions.

(A color version of this figure is available in the online journal.)

105 μas as the morphology uncertainty to be on the safer side. Based on the trigonometric parallax of 0.356 mas, 105 μas is 0.29 AU at PZ Cas. We conducted the combined fitting with all the maser spots whose positions were determined with JMFIT and obtained π^* of 0.356 ± 0.011 mas at this stage.

Note that the above error of the annual parallax is a result of considering the random statistical errors from the image S/N and the randomly changing maser spot position, as well as a common positional shift to all the maser spots at a specific epoch due to the astrometric error. Because the majority of the maser spots and features in the current parallax measurement are associated with the maser group a, the obtained stellar annual parallax could be affected by a time variation of the specific maser features at a certain level. Assuming that all the 13 maser spots belonging to group a have an identified systematic error, the annual parallax error can be evaluated to be $0.011 \times \sqrt{13} = 0.040$ mas. However, if we assume that maser spots belonging to a certain maser feature have a common systematic error but that some of them have their own time variations, the annual parallax error should be estimated to be ranging somewhere between 0.011 and 0.040 mas. To evaluate the contributions of such a systematic error, we carried out Monte Carlo simulations introduced by Asaki et al. (2010) for our astrometric analysis. First we prepared the imitated data set of the 16 maser spots with position changes added by considering the fixed stellar annual parallax and the maser proper motions. Second we added an artificial positional offset due to the image S/N, the astrometric accuracy, and the morphology uncertainty to each of the maser spot positions. The positional offset caused by the image S/N was given to each of the maser spots at each epoch independently. The positional offset due to the astrometric error was common to all the maser spots at a specific epoch but randomly different between the epochs. In this paper, we assumed that the positional offset due to the morphology uncertainty was common to all the maser spots belonging to a specific maser feature at a specific epoch, but randomly different between the features and the epochs. We assumed the standard deviation of the maser morphology uncertainty was 105 μas, equivalent to the intrinsic size of 0.29 AU. In a single simulation trial, we obtained the stellar annual parallax for the imitated data set. Thirdly we carried out 200 trials in order to obtain the standard deviation of the stellar annual parallax solutions. The resultant standard deviation was 0.026 mas which can be treated as the annual parallax error in our astrometric analysis. The resultant estimate of the stellar annual parallax was 0.356 ± 0.026 mas, corresponding to $2.81^{+0.22}_{-0.19}$ kpc.

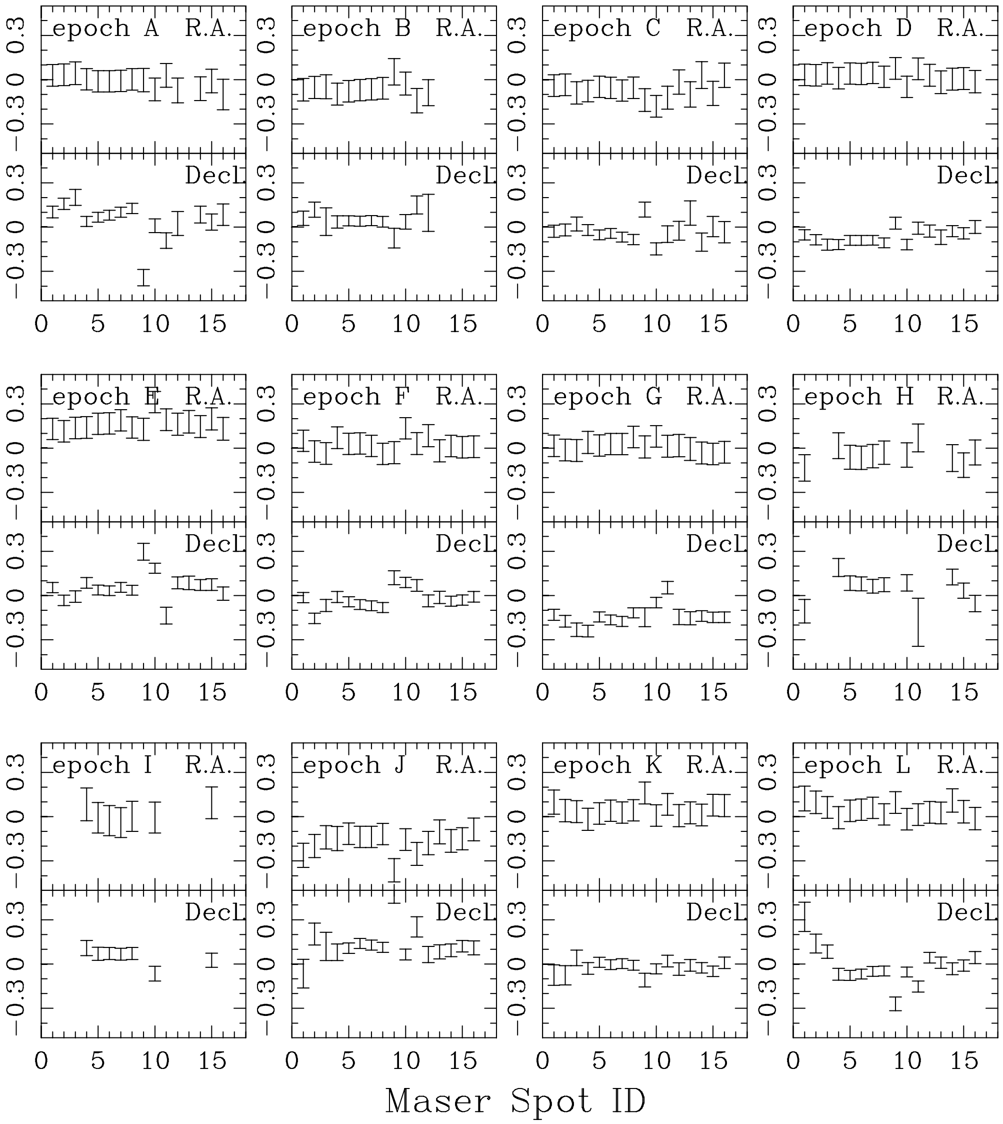

Figure 9. Position residuals of the 16 maser spots after removing the annual parallax of 0.356 mas, proper motions, and initial positions. The abscissa represents the maser spot ID as shown in Figures 6 and 7 and the ordinate is the position residual in mas. For each epoch, the position residuals in right ascension and declination are shown in the upper and lower panels, respectively.

4.2. Stellar Position and Proper Motion

Similar to the cases seen in other RSGs (VY CMa, Choi et al. 2008; S Per, Asaki et al. 2010; VX Sgr, Kamohara et al. 2005; Chen et al. 2006; NML Cyg, Nagayama et al. 2008; Zhang et al. 2012b), the maser features around PZ Cas are widely distributed over a 200 × 200 square mas (corresponding to 562 × 562 square AU at a distance of 2.81 kpc) while the velocity of the features (-52 to -37 km s^{-1}) is distributed more closely to the stellar systemic velocity than those found in other RSGs are. It is likely that the detected maser groups are located at the tangential parts of the shell-like circumstellar envelope, whose 3D velocity has a small line-of-sight velocity. We determined the proper motions of all detected maser spots were identified at least in two epochs. Table 6 lists maser spots whose proper motions and positions were calculated with the stellar annual parallax determined above. Using the proper motion data listed in Tables 5 and 6, we then conducted the least-squares fitting analysis to obtain the position of PZ Cas and the stellar proper motion based on the spherically expanding flow model (Imai et al. 2011). The obtained stellar proper motion in right ascension and declination, $\mu^*_\alpha \cos\delta = -3.7 \pm 0.2$ mas yr^{-1} and $\mu^*_\delta = -2.0 \pm 0.3$ mas yr^{-1}, respectively. The astrometric analysis result for PZ Cas is listed in Table 7. The proper motions of the detected maser spots together with the stellar position indicated by the cross mark are shown in Figure 10.

5. DISCUSSIONS

5.1. Distance to PZ Cas and Cas OB5

We obtained the trigonometric parallax to PZ Cas, $D = 2.81^{+0.22}_{-0.19}$ kpc as described in Section 4.1. PZ Cas is thought to be a member of the Cas OB5 association in the Perseus spiral arm. It is of interest to compare the distance to PZ Cas determined in this paper to distances that have been accepted by other methods. Mel'nik & Dambis (2009) estimated the trigonometric parallax to Cas OB5 to be 2.0 kpc from the median of trigonometric parallaxes of the member stars obtained with *Hipparcos*. Since a typical statistical error of *Hipparcos* annual parallaxes is ∼1 mas, we cannot fully rely on this statistical value for the

Table 6
Proper Motions and Initial Positions of the Maser Spots Detected in At Least Two Epochs[a]

Spot ID (Group ID)	$\Delta\alpha_A$ (mas)	$\Delta\delta_A$ (mas)	$V_{\rm LSR}$ (km s^{-1})	$\mu_\alpha \cos\delta$ (mas yr^{-1})	μ_δ (mas yr^{-1})
17(*a*)	-2.99 ± 0.09	49.94 ± 0.06	-40.5	-3.72 ± 0.24	-1.63 ± 0.11
18(*a*)	-2.99 ± 0.09	49.85 ± 0.06	-40.7	-3.60 ± 0.20	-1.57 ± 0.09
19(*a*)	-3.02 ± 0.08	49.79 ± 0.08	-40.9	-3.62 ± 0.20	-1.59 ± 0.10
20(*a*)	-3.05 ± 0.08	49.83 ± 0.09	-41.2	-3.67 ± 0.20	-1.64 ± 0.10
21(*a*)	-3.13 ± 0.09	49.99 ± 0.15	-41.4	-3.78 ± 0.27	-0.73 ± 0.11
22(*a*)	-4.36 ± 0.08	52.05 ± 0.05	-40.5	-3.87 ± 0.12	-1.45 ± 0.06
23(*a*)	-4.28 ± 0.07	52.09 ± 0.04	-40.7	-3.80 ± 0.07	-1.72 ± 0.03
24(*a*)	-3.78 ± 0.08	52.46 ± 0.07	-41.6	-3.81 ± 0.09	-1.29 ± 0.03
25(*a*)	-2.66 ± 0.09	56.15 ± 0.06	-41.2	-3.60 ± 0.08	-1.48 ± 0.04
26(*a*)	-1.42 ± 0.07	57.46 ± 0.04	-42.4	-3.59 ± 0.42	-1.79 ± 0.28
27(*a*)	-2.25 ± 0.07	56.82 ± 0.03	-42.2	-4.13 ± 0.19	-2.04 ± 0.09
28(*a*)	-2.19 ± 0.08	58.48 ± 0.05	-42.6	-3.70 ± 0.07	-1.82 ± 0.03
29(*a*)	-3.02 ± 0.10	61.42 ± 0.07	-42.6	-3.67 ± 0.13	-1.70 ± 0.04
30(*a*)	-3.04 ± 0.09	61.32 ± 0.04	-42.8	-3.84 ± 0.09	-1.59 ± 0.03
31(*a*)	-3.08 ± 0.08	61.35 ± 0.04	-43.3	-3.80 ± 0.08	-1.68 ± 0.03
32(*b*)	63.78 ± 0.09	-45.68 ± 0.06	-40.5	-1.71 ± 0.17	-3.08 ± 0.06
33(*b*)	63.92 ± 0.07	-45.71 ± 0.04	-40.7	-2.26 ± 0.07	-2.70 ± 0.03
34(*b*)	63.74 ± 0.08	-45.52 ± 0.05	-41.6	-2.34 ± 0.10	-2.85 ± 0.04
35(*b*)	60.50 ± 0.10	-44.46 ± 0.08	-41.2	-1.53 ± 0.70	-3.30 ± 0.04
36(*b*)	62.97 ± 0.08	-43.86 ± 0.05	-41.4	-2.70 ± 0.08	-2.31 ± 0.04
37(*b*)	63.00 ± 0.08	-43.74 ± 0.06	-41.6	-2.72 ± 0.10	-2.54 ± 0.04
38(*c*)	-31.47 ± 0.10	-66.14 ± 0.17	-42.0	-4.07 ± 0.17	-2.40 ± 0.05
39(*c*)	-31.48 ± 0.09	-66.14 ± 0.10	-42.2	-4.03 ± 0.15	-2.44 ± 0.05
40(*c*)	-33.02 ± 0.10	-67.47 ± 0.07	-42.4	-4.00 ± 0.30	-2.87 ± 0.06
41(*d*)	0.03 ± 0.08	77.85 ± 0.06	-48.3	-1.95 ± 1.44	-0.35 ± 0.17
42(*d*)	-0.06 ± 0.08	78.28 ± 0.06	-48.5	-3.42 ± 1.37	0.71 ± 0.17
43(*g*)	-3.97 ± 0.08	1.15 ± 0.05	-41.2	-3.77 ± 1.04	-1.95 ± 0.11
44(*g*)	-3.98 ± 0.08	1.06 ± 0.05	-41.4	-3.87 ± 0.27	-1.97 ± 0.05
45(*g*)	-3.89 ± 0.09	1.12 ± 0.06	-41.6	-4.00 ± 0.15	-1.98 ± 0.04
46(*g*)	-6.51 ± 0.09	0.67 ± 0.07	-41.8	-2.38 ± 1.61	-4.09 ± 0.05

Note.
[a] Maser spots listed in Table 5 are excluded.

Table 7
Astrometry Analysis Results of PZ Cas

Annual Parallax	$\pi^* = 0.356 \pm 0.026$ mas ($2.81^{+0.22}_{-0.19}$ kpc)	
Position (J2000)[a]	Right Ascension	Declination
(2006 Apr 20)	$23^{\rm h}44^{\rm m}03\overset{\rm s}{.}2816 \pm 0\overset{\rm s}{.}0004$	$+61^\circ 47' 22\overset{''}{.}187 \pm 0\overset{''}{.}003$
Stellar proper motion	$\mu_\alpha^* \cos\delta = -3.7 \pm 0.2$ mas yr^{-1}	$\mu_\delta^* = -2.0 \pm 0.3$ mas yr^{-1}

Note. [a] The position errors of J2339+6010 are not taken into consideration. This position is located at the origin of the PZ Cas image of Figure 5.

object. Another estimate of the distance to Cas OB5 is a distance modulus of 12, corresponding to the photometric parallax of 2.5 kpc (Humphreys 1978). VLBI phase-referencing astrometry has revealed that its measured trigonometric parallaxes for RSGs are well consistent with photometric parallaxes of the related star clusters within 10%–20% (S Per, Asaki et al. 2010; VY CMa, Zhang et al. 2012a; NML Cyg, Zhang et al. 2012b). Therefore, it is highly plausible that PZ Cas is involved in Cas OB5 from the geometrical viewpoint.

However, the difference between the distances derived from PZ Cas's annual parallax and the photometric parallax of Cas OB5 is too large to be explained from the viewpoint of its extent in depth, compared with the distribution on the sky of the member stars. One of the plausible reasons for the inconsistency is the overestimation of $A_{\rm V}$ to Cas OB5. If we attribute the inconsistency to the $A_{\rm V}$ value, the difference is 0.16 mag, which is comparable to a typical statistical error of $A_{\rm V}$. The *Gaia* mission is expected to yield measurements of accurate trigonometric distances for much more sampled stars than ever.

5.2. The Location of PZ Cas in the H-R Diagram

The bolometric luminosity, $L = 4\pi D^2 F_{\rm bol}$, of PZ Cas was estimated to be $2.0 \times 10^5 L_\odot$, $2.1 \times 10^5 L_\odot$, and $1.9 \times 10^5 L_\odot$ by Josselin et al. (2000), Levesque et al. (2005), and Mauron & Josselin (2011), respectively, with the distance modulus of Cas OB5 of 12 (Humphreys 1978). To derive the mass and age of PZ Cas, we first rescaled the luminosity values with our trigonometric parallax to $2.5 \times 10^5 L_\odot$, $2.7 \times 10^5 L_\odot$, and $2.4 \times 10^5 L_\odot$, respectively. Levesque et al. (2005) estimated the effective temperature of PZ Cas to be 3600 K from the MARCS stellar atmosphere models and the absolute spectro-photometry. Using this effective temperature, we ploted PZ Cas in the H-R diagram reported by Meynet & Maeder (2003), as shown in Figure 11. In this figure the filled circles represent the

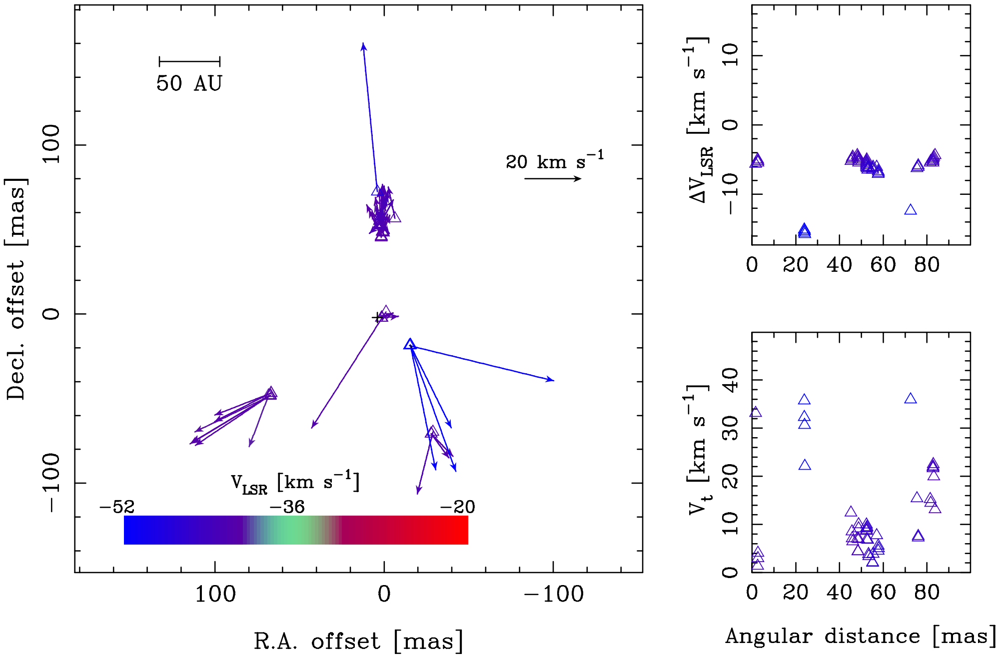

Figure 10. Internal motions of maser spots around PZ Cas. The cross bars around the map origin represent the position of PZ Cas and its positional error obtained with the least-squares fitting. The color represents the radial velocity and the open circles and triangles are red and blueshifted maser spots with respect to the systemic velocity. Left: spatial distributions of the maser spots with respect to the stellar position (coordinate origin). Top right: radial velocity–position plot. The abscissa is the angular distance from the stellar position, and the ordinate is the radial velocity difference from the systemic velocity. Bottom right: transverse velocity–position plot.

(A color version of this figure is available in the online journal.)

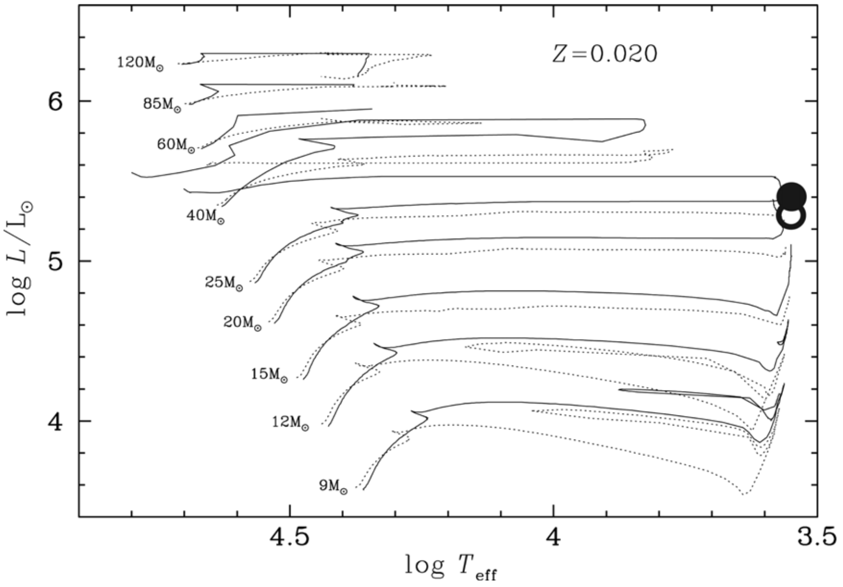

Figure 11. Locations of PZ Cas in the H-R diagram (Meynet & Maeder 2003). The open and filled circles represent the locations of PZ Cas estimated from the distance modulus and our trigonometric parallax, respectively. The effective temperature is assumed to be 3600 K (Levesque et al. 2005).

re-estimated luminosities based on Josselin et al. (2000), Levesque et al. (2005), and Mauron & Josselin (2011), while the open circles represent the originally reported ones. The luminosity previously estimated by using the distance modulus yields the initial mass of around 20 $M_\odot$ while, using our trigonometric parallax, it is estimated to be ∼25 $M_\odot$.

According to evolutionary tracks shown in Figures 1 and 2 of Meynet & Maeder (2003), the lifetime is estimated to be ∼8 Myr for an initial mass of 25 $M_\odot$ and ∼10 Myr for an initial mass of 20 $M_\odot$. Since the ages of four open clusters in Cas OB5 have been reported to be 120 ± 20 Myr for NGC 7790 (Gupta et al. 2000), and 30.2, 45.7, and 13.2 Myr for NGC 7788, Frolov 1, and King 12, respectively (Kharchenko et al. 2005), it is expected that PZ Cas was born after the first generation in Cas OB5.

5.3. Three-Dimensional Motion of PZ Cas in the Milky Way

The stellar proper motion and the radial velocity of PZ Cas enabled us to discuss its 3D motion in the Milky Way. In the analysis, we adopted the Galactocentric distance to the Sun of 8.5 kpc, and the flat Galactic rotation curve with the rotation velocity of 220 km s^{-1}. For the solar motion, we adopted the latest value obtained by Schönrich et al. (2010),

$11.10 \pm 0.75\,\mathrm{km\,s^{-1}}$ toward the direction of the Galactic center ($U_{\odot}$ component), $12.24 \pm 0.47\,\mathrm{km\,s^{-1}}$ toward the direction of the Galactic rotation ($V_{\odot}$ component), and $7.25 \pm 0.37\,\mathrm{km\,s^{-1}}$ toward the north pole ($W_{\odot}$ component). Since H_2O maser features around RSGs are spherically distributed, it is hardly plausible that an uncertainty in the stellar proper motion was caused by the anisotropic distribution, as those in the case of outflows of star-forming regions has to be considered (e.g., Sanna et al. 2009). Therefore, we did not introduce an additional uncertainty of the PZ Cas stellar motion other than the statistical error described in Section 4.2 in this error estimation. We followed the methods described by Johnson & Soderblom (1987) and Reid et al. (2009) to derive the peculiar motion and its error. The resultant peculiar motion of PZ Cas was (U_s, V_s, W_s)= (22.8 ± 1.5, 7.1 ± 4.4, -5.7 ± 4.4) $\mathrm{km\,s^{-1}}$.

Different from peculiar motions of Galactic high-mass star-forming regions (HMSFRs) typically showing negative V_s components (-10 to $-20\,\mathrm{km\,s^{-1}}$; e.g., Reid et al. 2009), PZ Cas has a large peculiar motion not in the V_s component but in U_s. At first, in order to discuss whether PZ Cas's peculiar motion is due to the internal motion inside Cas OB5, we investigated proper motions of the member stars of Cas OB5 using the *Hipparcos* catalog (Høg et al. 2000). Positions and velocities of Cas OB5 member stars (OB stars and RSGs) cataloged in Garmany & Stencel (1992) with compiled information from previous literatures (Evans 1967; Famaey et al. 2005; Fehrenbach et al. 1996; Humphreys 1970; Valdes et al. 2004; Van Leeuwen 2007; Wilson 1953) are listed in Table 8. Figure 12 shows the positions and proper motions of the member stars listed in Table 8 as well as stars with annual parallax <5 mas and proper motion <8 mas $\mathrm{yr^{-1}}$ in order to roughly exclude foreground stars. In Figure 12, the $J = 1 \rightarrow 0$ CO contour map of a Galactic plane survey (Dame et al. 2001) taken from *SkyView* (Internet's Virtual Telescope)[5] is superimposed. We obtained the unweighted average of those proper motions ($\mu_{\alpha} \cos\delta = -2.8 \pm 1.2$ and $\mu_{\delta} = -1.9 \pm 0.8$ mas $\mathrm{yr^{-1}}$) which is well consistent with Cas OB5's peculiar motion obtained by Mel'nik & Dambis (2009) ($\mu_{\alpha} \cos\delta = -3.8 \pm 1.2$ and $\mu_{\delta} = -1.4 \pm 0.8$ mas $\mathrm{yr^{-1}}$). Figure 13 shows 3D views of the relative positions and peculiar motions of PZ Cas and the member stars of Cas OB5 whose radial velocities can be found in previous literatures as listed in Table 8. Here we adopted PZ Cas's trigonometric distance for Cas OB5. The averaged peculiar motion of those member stars was ($\bar{U}$, $\bar{V}$, $\bar{W}$)=(8 ± 14, -1 ± 18, -9 ± 18) $\mathrm{km\,s^{-1}}$ whose U component was prominent comparing with the other two. Therefore, we concluded that the peculiar motion of PZ Cas with the large U_s component reflects Cas OB5's peculiar motion.

Why does PZ Cas, or Cas OB5, have such a large peculiar motion in the U component? Since the member stars including PZ Cas are located on the western side of a large shell-like structure molecular gas ($\mathrm{H_I}$ super shell) with the center position of a Galactic coordinate of (118°, −1°), one may consider that supernovae in precedent giant molecular clouds triggered the formation of those stars and that they have an expanding motion (Sato et al. 2008). We investigated *Hipparcos* proper motions of the member stars of Cas OB5, as well as those of Cas OB4 and Cas OB7 located on the eastern side of the shell-like structure, as shown in Figure 12. We also investigated 3D relative positions and peculiar motions of those of Cas OB4 and Cas OB7, as shown in Table 9. We adopted the photometric parallaxes for Cas OB4 and Cas OB7 reported by Garmany & Stencel (1992).

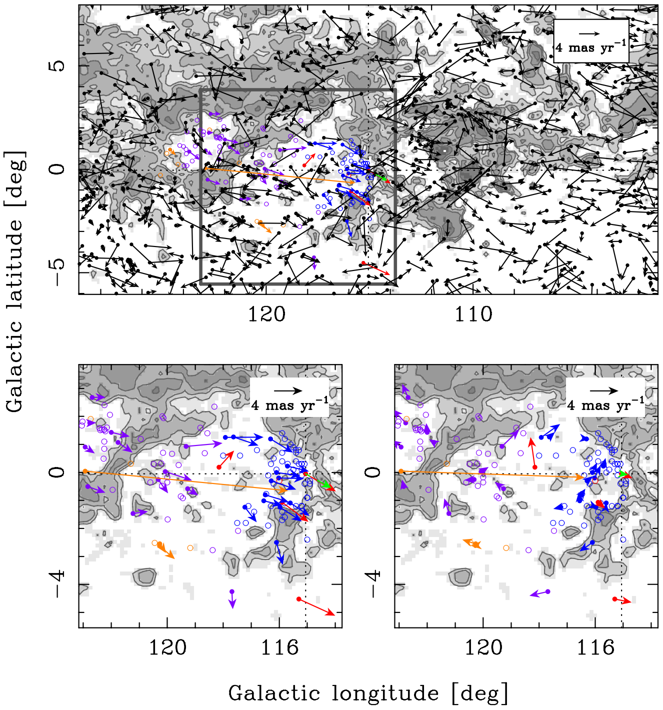

Figure 12. Top: proper motions of the Cas OB5, Cas OB4, and Cas OB7 members as well as stars with the annual parallaxes less than 5 mas and the proper motions less than 8 mas $\mathrm{yr^{-1}}$ in the *Hipparcos* catalog. The blue and red circles represent OB stars and RSGs, respectively, which have been identified as Cas OB5 members. The same goes for the Cas OB4 and Cas OB7. The purple and orange circles represent OB stars and RSGs, respectively. The filled and open circles denote the member stars found and not found in the *Hipparcos* catalog, respectively. The black points denote the stars whose proper motions are reported in the *Hipparcos* catalog but not identified with Cas OB5, Cas OB4, and Cas OB7 members. The arrows represent proper motions listed in the *Hipparcos* catalog. The position of PZ Cas is located at the crossing point of the horizontal and vertical dotted lines. The green arrow represents the proper motion reported in this paper. The background contour is the CO map reported by Dame et al. (2001). Bottom left: an enlarged picture of the area surrounded by the dashed square in the top panel. Bottom right: same as the bottom left panel, but the average proper motion of the Cas OB5 members was subtracted from each proper motion.

Figure 13 shows three-dimensional views of the positions and proper motions of the member stars of Cas OB5 as well as Cas OB4 and Cas OB7. We could hardly find clear evidence of an expanding motion of the member stars, either in the proper motions or the 3D motions between those three OB associations. One of the member stars of Cas OB7, HD 4842, has a much larger proper motion than those of the others, even if the *Hipparcos* trigonometric parallax of 1.46 ± 1.21 mas is considered. Therefore, this star could be a runaway star (Fujii & Zwart 2011).

VLBI astrometric observations of Galactic maser sources on Perseus spiral arm have revealed large peculiar motions of Galactic HMSFRs. According to Sakai et al. (2012), 33 sources whose peculiar motions have been measured in the Perseus and Outer arms show that these peculiar motions are almost located in the fourth quadrant in the U–V plane ($U > 0$ and $V < 0$). The peculiar motion of Cas OB5 is located in the fourth quadrant while that of PZ Cas is located in the first quadrant. Such a peculiar motion of the OB association may indicate the standard density wave theory (Lin & Shu 1964). However, it is hard to explain the velocity dispersion of the peculiar motions of the HMSFRs from the density wave theory.

---

[5] SkyView web: http://skyview.gsfc.nasa.gov/

Table 8
Proper Motions of the Member Stars of Cas OB5

Object	l[a] (deg)	b[a] (deg)	$\mu_\alpha \cos\delta$[a] (mas yr^{-1})	μ_δ[a] (mas yr^{-1})	V[b] (km s^{-1})	Spectral Type[c]
HD 223385	115.71	0.22	−2.80	−1.45	−55.7[d]	A3 I A+
HD 223767	116.02	−0.20	−3.51	−0.92	−38[e]	A4 I AB
HD 223960	115.97	−1.24	−2.57	−2.67	−48.1[f]	A0 I A+
BD +61 2550	116.08	0.04	−3.22	−1.25	−19[e]	O9.5 II
HD 224424	116.21	−2.45	−0.24	−3.31	−71[f]	B1 I AB
BD +62 2313	116.31	1.20	−2.67	−2.64	−53[e]	B3 I B
HD 224055	116.29	−0.30	−3.22	−1.99	−42.3[f]	B1 I A
LSI +61 106	116.47	−0.77	−3.07	−1.71		B1 V
HD 225146	117.23	−1.24	−1.27	−2.43	−29.0[f]	O9.7 I B
HD 225094	117.63	1.26	−3.27	−1.83	−43[f]	B3 I A
HD 108	117.93	1.25	−5.39	−0.93	−62.8[g]	O5F
ρ Cas	115.30	−4.52	−4.54	−3.45	−43.1[f]	F8 I ap
KN Cas	118.15	0.19	−2.50	2.02	−87.3[h]	M1 I bep+B
TZ Cas	115.90	−1.07	−3.05	−3.56	−54.28[i]	M2 I ab
PZ Cas	115.06	−0.05	−3.52	−3.55	−45.68[i]	M4 I a

Notes.
[a] Van Leeuwen (2007).
[b] Radial velocity (heliocentric coordinate).
[c] Garmany & Stencel (1992).
[d] Valdes et al. (2004).
[e] Fehrenbach et al. (1996).
[f] Wilson (1953).
[g] Evans (1967).
[h] Humphreys (1970).
[i] Famaey et al. (2005).

Table 9
Proper Motions of the Member Stars of Cas OB4 and Cas OB7

Object	l[a] (deg)	b[a] (deg)	$\mu_\alpha \cos\delta$[a] (mas yr^{-1})	μ_δ[a] (mas yr^{-1})	V[b] (km s^{-1})	Spectral Type[c]
Cas OB4						
HD 1544	119.27	−0.58	−1.38	−1.11	−52.0[d]	B0.5 III
HD 2451	120.32	−0.25	−1.22	−2.11	−37[d]	B0.5 IV
HILTNER 8	117.69	−4.25	0.25	−2.49	−23.5[e]	O9 IV
DL Cas	120.27	−2.55	−0.75	−1.38	−36.80[f]	F7.5 I B
HD 236433	120.28	−2.61	−2.02	−2.12	−11.2[g]	F5 I B
Cas OB7						
HD 3940	122.00	1.44	−2.61	−0.69	−48.0[h]	A1 I A
HD 4694	122.77	1.77	−0.90	0.04	−49.0[i]	B3 I A
HD 4841	122.93	0.91	−1.37	−0.93	−26[e]	B5 I A
HD 5551	123.71	0.85	−2.05	−1.53	−51.0[d]	B1.5 I A
HD 4842	122.93	0.05	−28.98	−2.81	−92[e]	M
HD 6474	124.65	0.95	−1.17	−1.00	−48.3[j]	G4 I A

Notes.
[a] Van Leeuwen (2007).
[b] Radial velocity (heliocentric coordinate).
[c] Garmany & Stencel (1992).
[d] Evans (1967).
[e] Wilson (1953).
[f] Mermilliod et al. (2008).
[g] Kraft (1958).
[h] Münch (1957).
[i] Abt et al. (1972).
[j] Humphreys (1970).

Such a large velocity dispersion in peculiar motions can be seen for the Galactic OB associations within 3 kpc from the Sun (Mel'nik & Dambis 2009). The peculiar motion of Cas OB5 hits upon an interesting idea of "time-dependent potential spiral arms'. Baba et al. (2009) reported on results of large N-body and smoothed particle hydrodynamics (SPH) simulations that calculated the motions of multi-phase, self-gravity gas particles in self-induced stellar spiral arms in a galactic disk. In their simulations, spiral arms are developed by the self-gravity but cannot keep their forms even in one galactic rotation evolution.

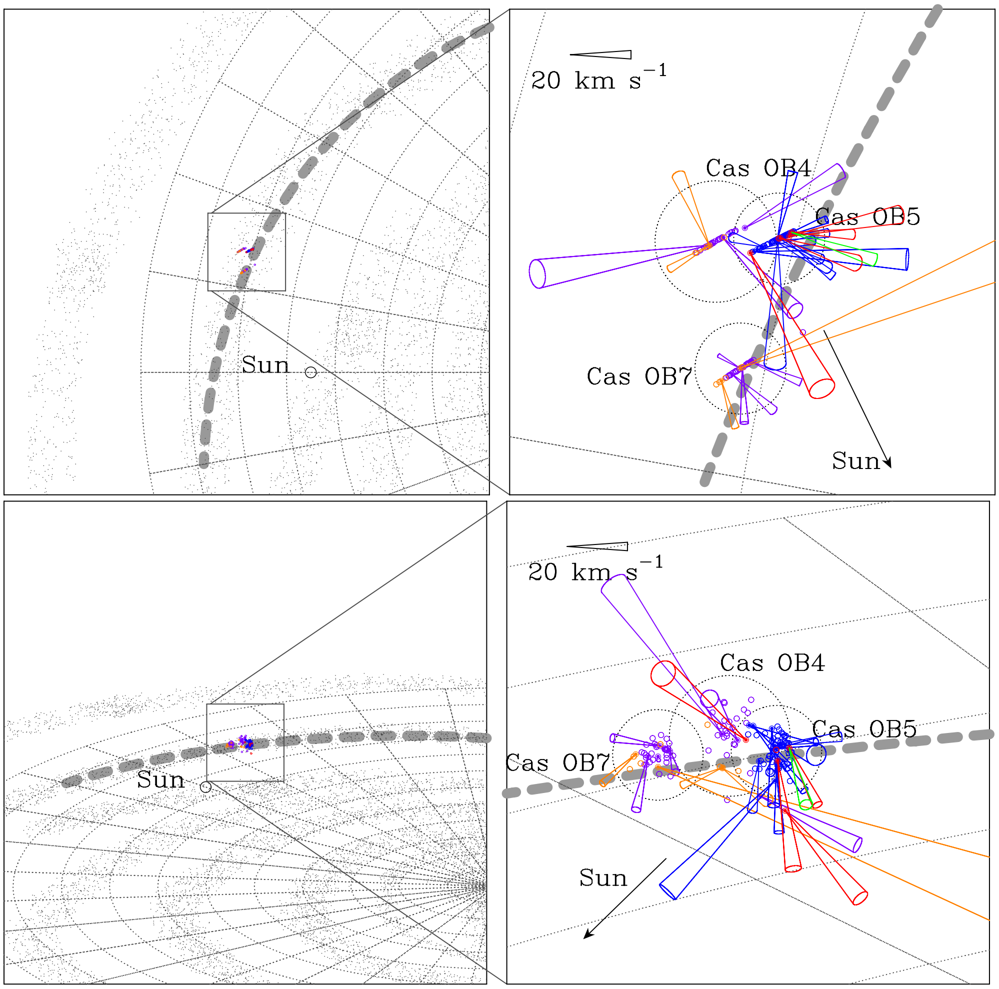

Figure 13. Three-dimensional views of the positions and peculiar motions of the member stars of Cas OB5 as well as Cas OB4 and Cas OB7. Note that the distance to Cas OB5 is assumed to be 2.8 kpc (this paper) while those of Cas OB4 and Cas OB7 are assumed to be 2.9 and 2.5 kpc, respectively, determined from the photometric parallaxes (Humphreys 1978). The blue and red points are OB stars and RSGs of Cas OB5, respectively, listed in Table 8. The green point represents PZ Cas's peculiar motion obtained in this paper. The purple and orange points are OB stars and RSGs of the other two OB associations, respectively, listed in Table 9. Conicals in the enlarged right plots represent the peculiar motions of the member stars after removing the flat Galactic rotation curve of 220 km s^{-1}. A thick gray dashed line represents the position of the Perseus spiral arm (Asaki et al. 2010).

Other simulation results by Wada et al. (2011) suggest that a massive cloud falls into a spiral arm's potential from both sides, that is, there are flows of cold gas with various velocities. The flows converge into condensations of cold gas near the bottom of the potential well. The relative velocities of the gas to the stellar spirals are comparable to the random motion of the gas. Another interesting point reported by Wada et al. (2011) is that supernovae feedback is not essential to change the velocity field of the gas near the spiral potential. Each of the cold massive clouds and stars with ages younger than 30 Myr may have a peculiar motion with a velocity dispersion of $\sim$30 km s^{-1}, which is not predicted by the density wave theory. Although we have not had samples large enough to discuss the whole structure of the Milky Way, the self-consistent gravity spiral galaxy model can explain those peculiar motions of HMSFRs in the Milky Way. In other words, a live spiral structure model can fit to the recent sample of the HMSFRs' spatial motions including Cas OB5. A deep understanding of the dynamics of the Galactic spiral arms and the origin of the peculiar motions of HMSFRs will be possible in the near future when massive numerical simulations can be combined with much larger VLBI astrometric samples which only can be conducted toward the Galactic plane obscured by dense gas.

6. CONCLUSIONS

We have conducted phase-referencing VLBI monitoring observations for the H_2O masers of the Galactic RSG, PZ Cas. The distance to PZ Cas was determined to be $2.81^{+0.22}_{-0.19}$ kpc from the derived annual parallax in the maser spot motions. We estimated the initial mass of PZ Cas as $\sim 25\ M_\odot$ using the rescaled stellar luminosity with the annual parallax.

Together with the stellar radial velocity and obtained proper motion, we investigated the 3D motion of PZ Cas in the Milky Way, showing the non-circular motion with a rather large velocity toward the Galactic center. We compared the proper motion and 3D peculiar motion of PZ Cas with those of the member stars of Cas OB5 using the proper motions cataloged in *Hipparcos* and their radial velocities. We found that the motion of PZ Cas in the Milky Way is close to that of the OB association. This peculiar motion is not aligned with those of the Galactic HMSFRs. The observed peculiar motion supports a live spiral arm model recently revealed by large *N*-body/SPH numerical simulations.

The VERA/Mizusawa VLBI observatory is a branch of the National Astronomical Observatory of Japan, National Institutes of Nature Sciences. The authors acknowledge the use of NASA's SkyView facility (http://skyview.gsfc.nasa.gov) located at NASA Goddard Space Flight Center. K. Kusuno was financially supported by the Center for the Promotion of Integrated Science of the Graduate University of Advanced Studies for this publication.

REFERENCES

Abt, H. A., Levy, S. G., & Gandet, T. L. 1972, AJ, 77, 138
Asaki, Y., Deguchi, S., Imai, H., et al. 2010, ApJ, 721, 267
Asaki, Y., Sudou, H., Kono, Y., et al. 2007, PASJ, 59, 397
Baba, J., Asaki, Y., Makino, J., et al. 2009, ApJ, 706, 471
Chen, X., Shen, Z-Q., Imai, H., & Kamohara, R. 2006, ApJ, 640, 982
Choi, Y. K., Hirota, T., Honma, M., et al. 2008, PASJ, 60, 1007
Dame, T. M., Hartmann, D., & Thaddeus, P. 2001, ApJ, 547, 792
Evans, D. S. 1967, in IAU Symp. 30, Determination of Radial Velocities and their Applications, ed. A. H. Batten & J. F. Heard (London: Academic), 57
Famaey, B., Jorissen, A., Luri, X., et al. 2005, A&A, 430, 165
Fehrenbach, Ch., Duflot, M., Genty, V., & Amieux, G. 1996, BICDS, 48, 11
Fujii, M. S., & Zwart, S. P. 2011, Sci, 334, 1380
Garmany, C. D., & Stencel, R. E. 1992, A&AS, 94, 211
Gupta, A. C., Subramaniam, A., Sagar, R., & Griffiths, W. K. 2000, A&AS, 145, 365
Hachisuka, K., Brunthaler, A., Menten, K. M., et al. 2006, ApJ, 645, 337
Høg, E., Fabricius, C., Makarov, V. V., et al. 2000, A&A, 355, L27
Honma, M., Fujii, T., Hirota, T., et al. 2003, PASJ, 55, L57
Honma, M., Hirota, T., Jike, T., et al. 2010, PNAOJ, 13, 57
Honma, M., Kijima, M., Suda, H., et al. 2008, PASJ, 60, 935
Humphreys, R. W. 1970, ApJ, 160, 1149
Humphreys, R. M. 1978, ApJS, 38, 309
Imai, H., Omi, R., Kurayama, T., et al. 2011, PASJ, 63, 1293
Johnson, D. R. H., & Soderblom, D. R. 1987, AJ, 93, 864
Josselin, E., Blommaert, J. A. D. L., Groenewegen, M. A. T., Omont, A., & Li, F. L. 2000, A&A, 357, 225
Kamohara, R., Deguchi, S., Miyoshi, M., & Shen, Z-Q. 2005, PASJ, 57, 341
Kerr, F. J., & Lynden-Bell, D. 1986, MNRAS, 221, 1023
Kharchenko, N. V., Piskunov, A. E., Röser, S., Schilbach, E., & Scholz, R. D. 2005, A&A, 438, 1163
Kraft, R. P. 1958, ApJ, 128, 161
Levesque, E. M., Massey, P., Olesn, K. A. G., et al. 2005, ApJ, 628, 973
Lin, C. C., & Shu, F. H. 1964, ApJ, 140, 646
Mauron, N., & Josselin, E. 2011, A&A, 526, A156
Mel'nik, A. M., & Dambis, A. K. 2009, MNRAS, 400, 518
Mermilliod, J. C., Mayor, M., & Udry, S. 2008, A&A, 485, 303
Meynet, G., & Maeder, A. 2003, A&A, 404, 975
Münch, G. 1957, ApJ, 125, 42
Nagayama, T., Takeda, K., Omodaka, T., et al. 2008, PASJ, 60, 1069
Petrov, L., Hirota, T., Honma, M., et al. 2007, AJ, 133, 2487
Reid, M. J., Menten, K. M., Zheng, X. W., et al. 2009, ApJ, 700, 137
Reid, M. J., & Moran, J. M. 1981, ARA&A, 19, 231
Richards, A. M. S., Etoka, S., Gray, M. D., et al. 2012, A&A, 546, A16
Rioja, M., Dodson, R., Asaki, Y., Hartnett, J., & Tingay, S. 2012, AJ, 144, 121
Sakai, N., Honma, M., Nakanishi, H., et al. 2012, PASJ, 64, 108
Sanna, A., Reid, M. J., Moscadelli, L., et al. 2009, ApJ, 706, 464
Sato, M., Hirota, T., Honma, M., et al. 2008, PASJ, 60, 975
Schönrich, R., Binney, J., & Dehnen, W. 2010, MNRAS, 403, 1829
Valdes, F., Gupta, R., Rose, J. A., Singh, H. P., & Bell, D. J. 2004, ApJS, 152, 251
van Leeuwen, F. 2007, A&A, 474, 653
Wada, K., Baba, J., & Saitoh, T. R. 2011, ApJ, 735, 1
Wilson, R. E. 1953, General Catalogue of Stellar Radial Velocities (Washington, DC: Carnegie Institute of Washington)
Zhang, B., Reid, M. J., Menten, K. M., & Zheng, X. W. 2012a, ApJ, 744, 23
Zhang, B., Reid, M. J., Menten, K. M., Zheng, X. W., & Brunthaler, A. 2012b, A&A, 544, A42